RESEARCH ARTICLE

ADVANCED
INTELLIGENT
SYSTEMS
Open Access

www.advintellsyst.com

A Voxel-Based Approach for the Generation of Advanced Kinematics at the Microscale

Gilles Decroly,* Adam Chafaï, Guillaume de Timary, Gabriele Gandolfo, Alain Delchambre, and Pierre Lambert

In soft robotics, the ability to generate advanced kinematics is a necessary step toward any more sophisticated tasks such as microobject manipulation, locomotion, or configuration changes. To this end, herein, a modular voxel-based methodology adaptable to any scale and with any soft transducer is presented. The methodology is implemented at the micrometer scale with a one-step fabrication process. An innovative gray-tone lithography method using the two-photon polymerization of photosensitive poly(*N*-isopropylacrylamide) hydrogel is developed to print the voxels. Bending, compression, and twisting voxels are designed, printed, and characterized. A voxel consists of an isotropically shrinking active material reinforced adequately with a passive pattern. Each elementary voxel deforms along one degree of freedom and is a building block for superstructures able of advanced kinematics. With a side length of 40 µm, the bending voxel achieves a bending angle of 25° or curvature of 10 mm^{-1}. The compression voxel reaches an actuation strain of 40%, and the twisting voxel bends up to 18°. Advanced kinematics are demonstrated by printing complex structures composed of multiple elementary voxels. Herein, a foundation toward soft microrobots capable of performing complex tasks is constituted.

1. Introduction

Soft active matter has gained increased interest as a source material for the fabrication of microactuators.[1–4] A key step

in achieving more sophisticated tasks, such as microobject manipulation, locomotion, or configuration change, is to control their ability to generate advanced kinematics. We define here advanced kinematics or complex motions as deformations beyond pure elongation, compression, shear, twist, or bending. To this end, several strategies have recently been proposed,[5–9] which would benefit from a formalized design methodology. In the previous work,[10] we proposed the following framework to analyze and compare the variety of solutions presented in the literature: First, a motion is generated using a stimuli-responsive material by supplying energy to a transducer with a stimulus, typically heat, light, or pressure. Second, under this stimulus, the transducer (stimuli-responsive material or structure) produces mechanical work, i.e., force and displacement. Third, asymmetry must be introduced into the system to program kinematics beyond isotropic expansion or shrinking. This asymmetry can be integrated through the stimulus if the latter is directed/inhomogenous. If the stimulus is isotopic, asymmetry can also come from the transducer or the material itself: isotropic transducers will expand or shrink uniformly under a stimulus, whereas anisotropic transducers present an intrinsic asymmetry. Fourth, passive or active mechanical asymmetric constraints can also be added to guide the deformation of the actuator. In addition, we proposed three classes of strategies to generate complex motions from basic kinematics relying on 1) the multiplication of stimuli or transducers; 2) the exploitation of nonlinear transducer responses or structured controlled stimuli; 3) and the modular decomposition of the complex motions into their basic constitutive kinematics (i.e., elongation, compression, shear, twist, or bending). Among these strategies, the modular approach based on voxels, i.e., elementary active structures, appeared interesting for its versatility.[10]

Zhang et al.[11] reviewed the basic principles of this approach. Bending, twisting, expansion, and contraction (McKibben-like actuators) can be easily generated and have been widely reported.[10,12] In our previous work, we showed that shear could also be obtained at the centimeter scale using an isotropically expansive transducer.[13] Advanced modular robots have been engineered using similar voxel-based approaches, with either predefined bending or twisting modules[14] or reprogramable

G. Decroly, A. Chafaï, G. de Timary, P. Lambert
TIPs Dpt CP 165/67
Université Libre de Bruxelles
Av. F. Roosevelt 50, B-1050 Brussels, Belgium
E-mail: gilles.decroly@ulb.be

G. Decroly, A. Delchambre
BEAMS Dpt CP 165/56
Université Libre de Bruxelles
Av. F. Roosevelt 50, B-1050 Brussels, Belgium

G. Gandolfo
Laboratory of Polymeric and Composite Materials
University of Mons
20 Pl. du Parc, B-7000 Mons, Belgium

**ADVANCED
SCIENCE NEWS**

www.advancedsciencenews.com

**ADVANCED
INTELLIGENT
SYSTEMS**

www.advintellsyst.com

voxels which can bend, contract, and stiffen.[15] Both solutions rely on pneumatic actuation and are implemented at the centimeter scale. Khodambashi et al.[16,17] built complex grippers made of hydrogel-based voxels, individually actuated using Joule heating. Similarly, Sun et al.[18] proposed a machine learning-based method to design active beams capable of adopting complex configurations with 50 µm side length voxels. These voxels only compress isotropically, and the asymmetry is introduced at the assembly level.

At the micrometer scale, poly(N-isopropylacrylamide) (pNIPAM) hydrogel-based actuators have been identified as promising miniaturizable isotropically shrinking transducers, suitable for digital fabrication and capable of developing high actuation strain.[19–22] pNIPAM-based transducers can be printed in one step using two-photon polymerization, where the polymerization of the pNIPAM resist is initiated locally using a femtosecond laser pulse[23] or using similar fabrication processes.[19,20] This way, complex-shaped structures can be obtained. Tang et al.[22] identified four types of principles to generate the actuation: using bilayer, gradient, or patterned structures; or using a localized stimulus. The resulting deformations are mainly restricted to the bending of tubular structures or to the change in the configuration of planar structures (to develop helixing or Gaussian curvatures).[22] To move further toward the generation of advanced kinematics, Huang et al.[24] arranged bilayer elements into programable building blocks at the micrometer scale that can be easily assembled into superstructures. However, these approaches rely on simple bilayers or isotropically compressive voxels, and the programing of the kinematic is introduced at the assembly level. Consequently, they are difficult to generalize to any shape and any motion.

In this work, we introduce and implement a modular voxel-based methodology at the micrometer scale with a one-step fabrication process using the two-photon polymerization of a photosensitive pNIPAM hydrogel. We aim to build on these previous works by implementing new degrees of freedom in individual voxels. The voxel-based approach is schematized in **Figure 1**. Any isotropically expansive or shrinking transducer (Figure 1a) is reinforced with an external pattern (Figure 1b) to form an elementary cubic structure called voxel (Figure 1c). Voxels deform according to single kinematics or degree of freedom (bending, torsion, shearing, elongation, or compression), mechanically programed by the design of the external reinforcement pattern. The latter should be 1) passive, 2) asymmetric, and 3) stiffer than the active matter. Voxels can then be assembled as building blocks to shape complex continuous superstructures capable of achieving advanced kinematics (Figure 1d). We present an innovative gray-tone lithography method to implement these pNIPAM-based voxels actuators at the micrometer scale. Voxels are designed, implemented, characterized, and combined into complex motions. The originality of this work comes from the additional layer of mechanical programing, at the voxel level, which enables to build of more modular structures by simply assembling individual voxels while limiting the space requirement and increasing their energy density.

2. Results

2.1. Design and Implementations of the Voxels

The structures are printed using two-photon polymerization with pNIPAM. pNIPAM is a thermo-responsive hydrogel. When swelled in water, it shows important shrinking when heated above its lower critical solution temperature (LCST) of 33 °C. Up to 300% actuation strain was reported in the literature.[25] To build stiffness or thermo-responsiveness gradients and introduce anisotropy to the printed structure, the mechanical properties of the printed material can be locally modulated by adapting the fabrication parameters.[7,24–27] This strategy is called gray-tone lithography. The mechanical properties of the material are related to its crosslinking density, which can be fine-tuned by modifying the composition of the resist or by varying the exposure dose throughout the printing.[7,25] The degree of reticulation, i.e., the cross-linking rate between the polymer chains, increases with the exposure dose. The more reticulated the
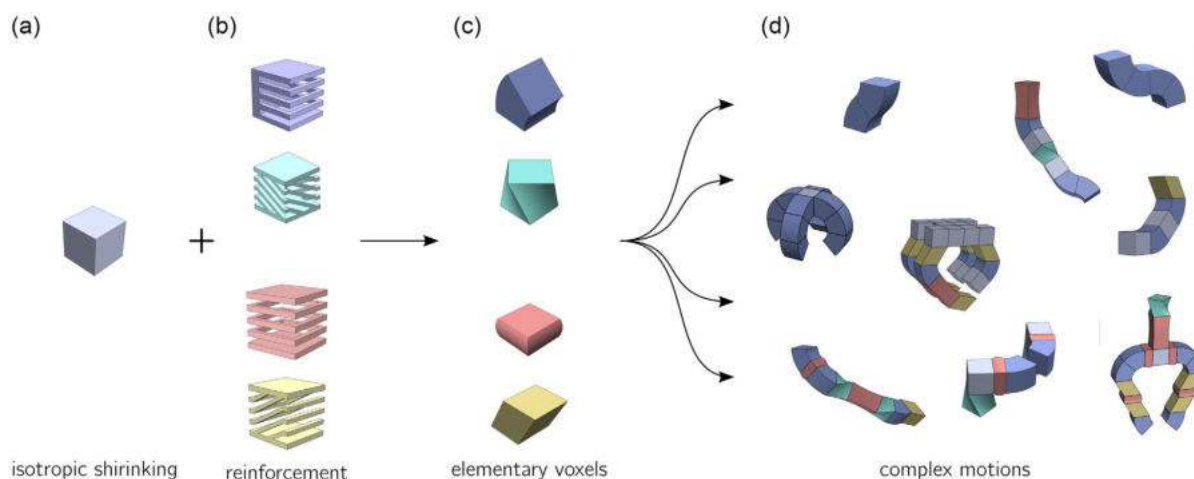

Figure 1. Principles of the voxel-based approach. A voxel is made of a) an isotropically shrinking active material and b) reinforced adequately with a passive pattern. This approach can also be implemented with expansive material. c) Each elementary voxel deforms along one degree of freedom and is a building block for superstructures. d) Complex motions can be obtained by assembling the voxels.

polymer, the more rigid the material, the less it swells in water, and hence the less it shrinks when heated above the LCST.[28] Its mechanical properties are also modified as the pNIPAM contracts. When swollen at rest, because of the water captured in the network, the overall structure is softer than when shrinked.[28] Note that other work used a similar fabrication process with pNIPAM-based photoresists of various compositions[29,30] or used pNIPAM with other fabrication processes.[31–33]

The pNIPAM hydrogel resists recipe is inspired by Hippler et al.[25,28]. The same proportions of NIPAM, crosslinker, and solvent are kept. The mass fraction of photo-initiator is doubled to decrease the exposure dose needed for polymerization.[34] Details are given in Section 4. For a given formulation, the mechanical properties of pNIPAM are related to its degree of reticulation, which is a function of the exposure dose, which is depends on two physical parameters: the laser power P and the laser velocity v. As a rule of thumb, the dose D can be estimated as $D \sim P^2/v$.[35] The power is set to its maximal value (50 mW) to minimize the printing time, and the laser velocity is used as the control parameter for the reticulation rate. Note that the degree of reticulation obtained for a given laser velocity also depends on the exact resist formulation, the hatching and slicing distances, the objective, and the overlap.[35,36] Hu et al.[36] thoroughly studied this influence for commercial resists. As illustrated in **Figure 2**a, the structures are built as an assembly of

elementary cubes of 5 μm side with an overlap of 1.5 μm to ensure their cohesion. Details can be found in Section 4.

The designs of the individual voxels are presented in Figure 2b–g. The designs aim to be as general as possible, i.e., to be adaptable to any shrinking or expansive transducer. Hence, the reinforcement is only added to the external contour of the voxels. They are made of an assembly of $10 \times 10 \times 10$ elementary cubes and placed in a cantilever on a highly reticulated base. This configuration enables to observe their deformation from the top. Note that with the overlap, the theoretical side dimension of the voxels is 36.5 μm. In addition to the basic kinematics, nonreinforced and bilayer voxels are implemented (Figure 2b,c). Nonreinforced voxels are used to characterize the influence of the printing parameters and temperature on the free actuation strain, and bilayer voxels serve as a reference since this design has been widely used in the literature and with similar hydrogel.[25] The designs of the bending and compression voxels are quite straightforward (Figure 2d,e). For the compression voxel, the reinforcement pattern consists of one layer of elementary cubes polymerized with a higher dose. Each ring of reinforcement is separated by one elementary cube, which is less reticulated. The reinforcement pattern of the bending voxel is similar to the compression voxel, to which a backbone is added on one side. This 8.5 μm thick backbone, or strain limiting layer, is made of two layers to increase its compression stiffness while limiting its bending stiffness. Twisting (Figure 2f) has been
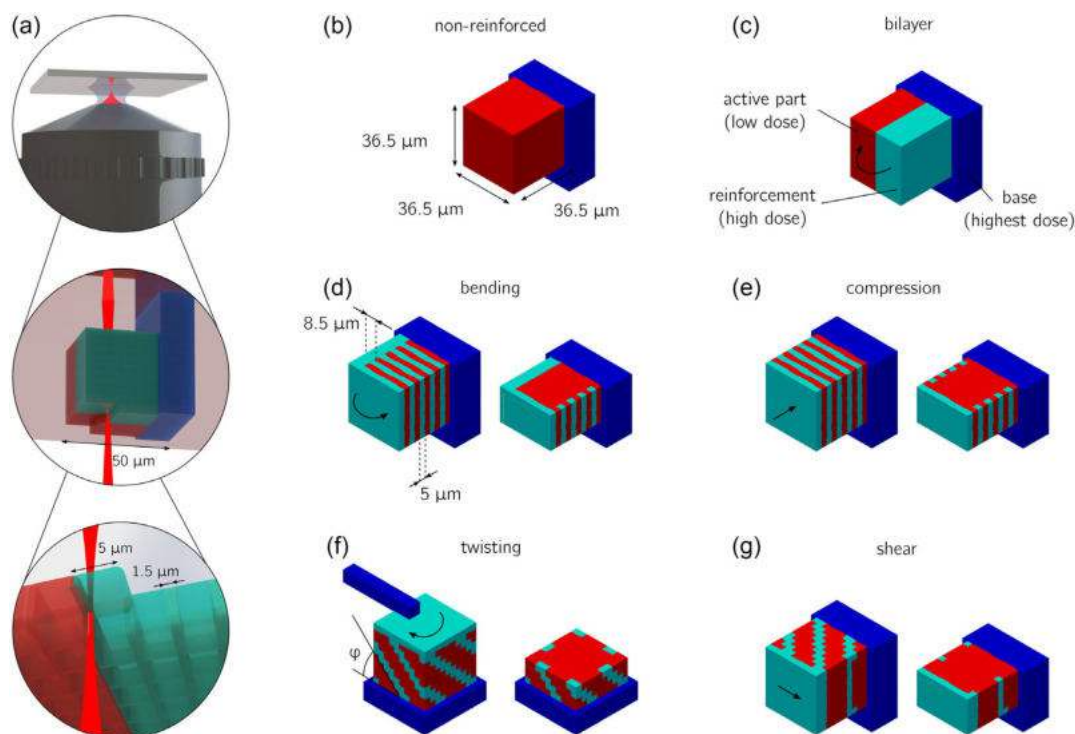

Figure 2. pNIPAM voxels are printed using two-photon polymerization. a) The printing strategy consists of decomposing the voxel in elementary cubes of 5 μm side length. These cubes are printed side-by-side with an overlap of 1.5 μm, which enables to control the degree of reticulation of each elementary cube independently. The designs of the voxels are shown as printed on the glass substrate. The distinct colors indicate the degree of reticulation of each part. b) The nonreinforced voxel is used to measure the free actuation strain, and c) the bilayer structures to compare the results to the literature. The d) bending, e) compression, f) twisting, and g) shear voxels are shown entirely (left) and with a horizontal cut view to show their internal structure (right). The top rod of the twisting voxel serves as a reference to observe the deformation when actuated.

widely studied with isotropically expansive transducers reinforced with fibers. The reinforcement angle φ is known for its influence on the generated twist, with a maximum for a reinforcement angle around 30° or expansive transducers.[12] Here, the transducer is isotropically shrinking, and the angle of the reinforcement is limited by the discretization induced by the elementary cubes approach. Consequently, the reinforcement angle is set to $\varphi = 45°$. Concerning the shear voxels (Figure 2g), similar designs have never been reported in the literature to our knowledge. As for the twisting voxel, the design is restricted by the discretization induced by the elementary cubes. The highly reticulated base is printed with a slow laser velocity of $4\,\mathrm{mm\,s^{-1}}$. For the reinforcement patterns, which should be stiffer and thereby show less contraction when heated, the printing laser velocity ranges from 5 to $9\,\mathrm{mm\,s^{-1}}$. Finally, the laser velocity used to print the active parts is varied between 10 and $16\,\mathrm{mm\,s^{-1}}$. The printing time ranges from 15 to 30 min depending on the voxel.

A finite element model (FEM) is built to qualitatively explore and validate the obtained kinematics of the voxels designs (**Figure 3**a–e). This FEM does not aim at modeling precisely the behavior of the voxels. The model is strongly inspired by Hippler et al.[25,28]. Several hypotheses are made: the overlap between the elementary cubes and the pixelization of the structures are not implemented, the material is considered linear elastic, and the influence of the temperature on the materials Young's modulus is not taken into account. With these assumptions, the implemented geometries are shown in Figure 3. Details are given in Section 4. Note that the results are not fitted on the experimental results. It would be possible to use the free actuation strain as fitting parameter.[25] However, this is not necessary regarding our objective of qualitatively validating the kinematics obtained for the different voxels, and it would bring no additional information. The FEM validates the implemented geometries by showing that the targeted kinematics can be

achieved. Among the desired deformations, i.e., the deformations along the intended degree of freedom, a displacement or angle is measured for each type of voxel. From these quantities, curvature or strain is computed. The bending can be assessed by measuring an angle θ_b (Figure 3f). A curvature $k = \theta_b/h_0$ and a strain $\varepsilon = kb_0/2$ can also be derived from the angle θ_b and the initial height h_0 and width b_0 of the voxels by considering the most elongated fiber under the hypothesis of constant curvature. The compression is characterized by the average vertical displacement of the top face d_z (Figure 3g). Here, the actuation strain is here defined by d_z/h_0. The twisting angle θ_t is defined similarly to the bending (Figure 3h). Under the assumption of small deformations, the shear strain of the twisting voxel is defined as $\gamma = \theta_t b_0/2h_0$. Finally, the absolute deformation of the shear voxel is best characterized by the average horizontal displacement of the top face d_x, while the shear strain is defined by $\gamma = d_x/h_0$ (Figure 3i). In addition to these desired deformations, parasitic deformations are observed when the voxels are actuated. These parasitic deformations correspond to deformations of the voxels along undesired degrees of freedom and are schematized in Figure 3. These parasitic motions should be minimized toward a controlled voxel-based methodology. In particular, the top face should keep its initial dimension and remain planar to ease the assembly of the voxels. Radial compression $(b_0 - b)$ is observed on all the voxels. Axial compression $(h_0 - h)$ is observed for bending, twisting, and shear. Parasitic shear $(d_x \neq 0)$ is observed for bending.

2.2. PNIPAM Characterization

The actuation strain and cyclability of the printed pNIPAM are characterized using the non-reinforced voxels, with printing laser velocities for the body material ranging from 4 to $16\,\mathrm{mm\,s^{-1}}$. The structures are actuated with a hot water bath. The experimental setup is described in Section 4. The shrinking at high
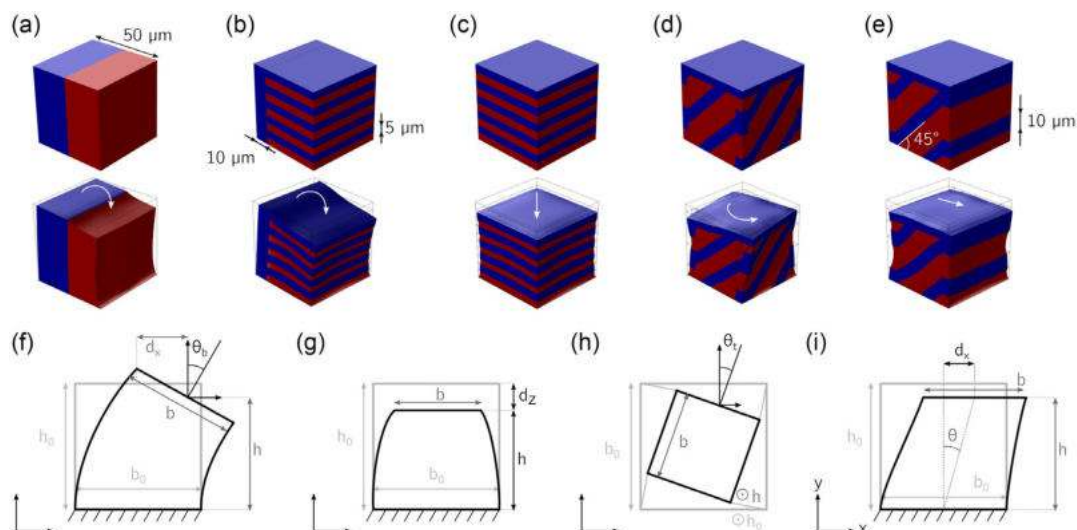

Figure 3. The voxels are implemented in COMSOL. The red indicates the active body material, and the reinforcement pattern is in blue: a) bilayer, b) bending, c) compression, d) twisting, and e) shear. The voxels are schematized below with the relevant metrics to characterize the desired and parasitic deformations. Lateral views of the f) bending, g) compression, and i) shear voxels. Top view of the h) twisting voxel. The initial shapes are indicated in light gray, with h_0 and b_0 being the initial height and width of the voxels. The deformed shapes are in black.
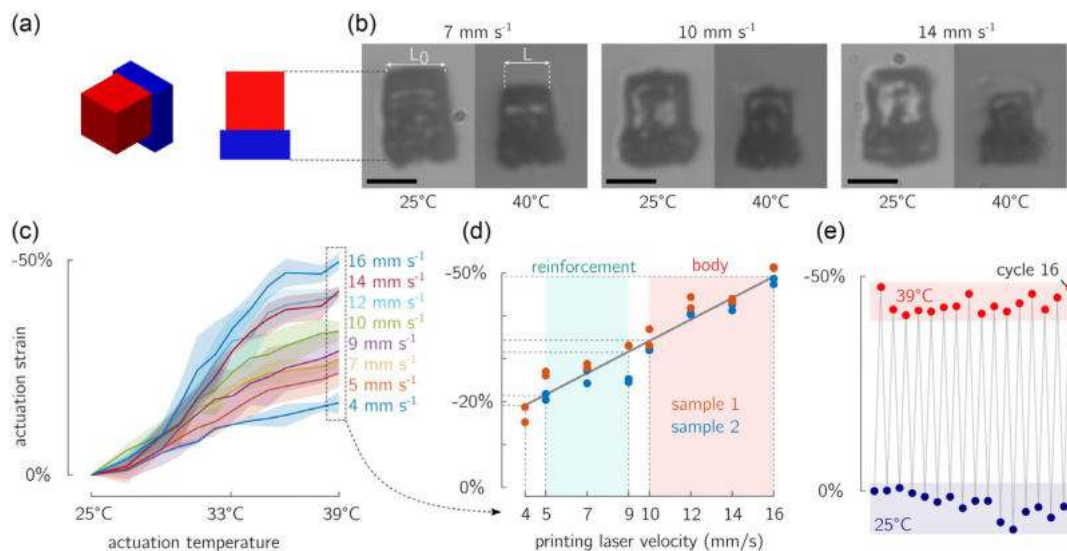
Figure 4. Free strain characterization. a) Structure design. b) When heated, the structure shrinks. c) The thermo-responsiveness is characterized as a function of the temperature-varying laser velocities, ranging from 4 to 16 mm s⁻¹. The shaded area shows the standard deviation obtained from two repeated measurements on two different samples for each degree. d) At 39 °C, the actuated strain depends linearly on the printing laser velocity. The shaded area represents the range of values chosen for the body and reinforcement parts of the voxels. Each data point corresponds to a single measurement. e) Cyclic actuation of the structure printed at 16 mm s⁻¹ shows no decrease in the actuation strain. Scale bar: 50 μm.

temperature can be observed in **Figure 4**a. The actuation strain is computed as $\varepsilon = \frac{L-L_0}{L_0}$, with L_0 corresponding to the voxel side length at 25 °C, and L being the actuated voxel side length. They are measured by taking the top corners of the voxels as references (Figure 4b). The actuation strain as a function of the temperature is represented in Figure 4c. The strain curve is coherent with the transition temperature (LCST) around 33 °C indicated in the literature.[25] At 39 °C, up to 50% compressive strain is measured for a printing laser velocity of 16 mm s⁻¹. Note that up to 300% compressive strain has been reported in the literature with similar hydrogel.[25] Several hypotheses can explain this difference: the resist formulation is not the same as the mass fraction of the photoinitiator is doubled to ease the fabrication process; the elementary cubes fabrication strategy could limit the compression strain by adding inhomogeneity in the voxels; and the 300% value is measured in a different configuration (structure height, one repetition, unknown printing parameters). The actuation strain at 39 °C is shown as a function of the printing laser velocity in Figure 4d. Each point represents one measure. The strain depends linearly on the laser velocity v and is thereby inversely proportional to the exposure dose. No optimum is observed in the experimental range of laser velocities. However, when increasing the velocity, the reticulation limit is reached, and the elementary cubes do not link to each other (Figure S1, Supporting Information). It is also interesting to note that when the base is printed with a laser velocity of 4 mm s⁻¹, the shrinking strain almost reaches 20% though local explosion occurs during the printing. The cyclability of pNIPAM actuation is also studied by measuring the actuation strain for 16 cycles on a structure printed with a laser velocity of 16 mm s⁻¹ (Figure 4e). No significant loss of capability is observed. Despite a small drift of the strain value, the stroke remains of the same order of

magnitude during the 16 cycles. The experimental error on the measure, discussed in Section 4, could explain these observations. These results are coherent with previous works, where up to 20 cycles were reported without any loss of capabilities.[37] However, even if no fatigue is observed, a decrease in the actuation capabilities has been observed for structure stored for three months. The response time is not investigated. The shrinking speed depends on the structure size as the actuation relies on the thermalization of the structure and the expulsion of the water out of it. Hippler et al.[25] estimated the actuation time of structures of similar dimensions to be of the order of magnitude of 100 ms when actuated through local heating with a 780 nm laser. The response time should be characterized in future work. However, it is not foreseen as a limitation toward microrobotics application.

2.3. Voxels Characterization

The deformations of the functionalized voxels are measured at 40 °C. The experimental design is shown in **Figure 5**a,b for the bending voxel, and the printed structures in Figure 5c. When printing with pNIPAM, the swelling during fabrication is important to consider.[27] Up to 18% swelling has been observed when comparing the dimensions of the obtained voxels with the designed 36.5 μm side length. The results of the bilayer characterization are shown in Figure 5d. A stop motion of the actuation of the voxels can be found in the Video, Supporting Information. The two corners of the top surfaces are taken as a reference for the angle measurement. A flexion of up to 24.8° is obtained with printing laser velocities of 7 mm s⁻¹ for the reinforcement and 14 mm s⁻¹ for the body. Considering a cubic voxel side length L_0 of 40 μm (i.e., the size of the printed

ADVANCED
SCIENCE NEWS
www.advancedsciencenews.com

ADVANCED
INTELLIGENT
SYSTEMS
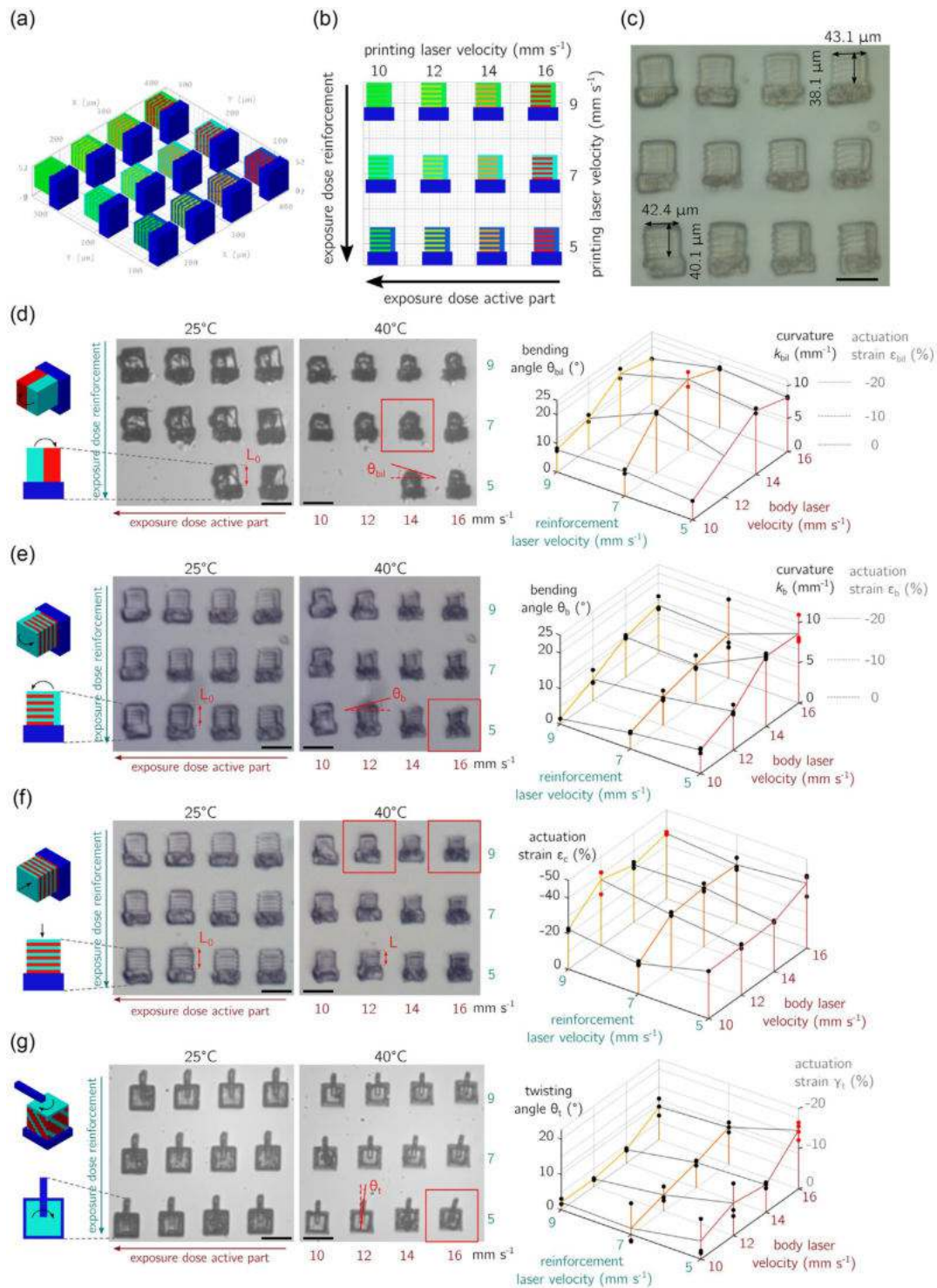Open Access

www.advintellsyst.com

Figure 5. Voxels characterization. a) Experimental design of prints: 3D view. b) Top view. The voxels are placed such as one line corresponds to one printing laser velocity of the reinforcement, and one column corresponds to one printing laser velocity for the active body. For example, the printing laser velocities for the voxel on the top right are respectively 16 and 9 mm s^{-1}. These laser velocities are also indicated by the colors of each voxel. Note that the exposure dose is inversely proportional to the laser velocity. c) Structures are observed and measured with a confocal microscope (Keyence VK-X200). d–g) Deformation of the voxels for different laser velocities combinations: d) bilayer, e) bending, f) compression, and g) twisting. The images are made with the characterization test bench, and the measures as indicated in red. The red boxes and red data points correspond to the structures showing the maximal strain. See Figure S2, Supporting Information, for detailed graphs. Scale bar: 50 µm.

and swelled voxels, as shown in Figure 5c), an equivalent curvature k_{bil} and actuation strain ε_{bil} can be computed with $k_{bil} = \theta_{bil}/L_0$ and $\varepsilon_{bil} = k.L_0/2$. For the optimal printing laser velocities combinations, they amount to, respectively, $k_{bil} = 10.8\,mm^{-1}$ and $\varepsilon_{bil} = -21.6\%$. The negative strain value indicates a compressive strain. This is coherent with previous work that reported curvature up to $15\,mm^{-1}$ for bilayer structures, having however a higher aspect ratio.[25] Here, the shortness of the cubic beam induces edge effects due to the constrains at the connection with the base, limiting the bending. A maximum is observed inside the parameter space—both for the reinforcement and for the body. For the reinforcement, if the backbone is too reticulated, it will be stiffer, and the actuation stress of the active part will not be sufficient to bend it. On the other side, if it is not reticulated enough, its actuation strain becomes nonnegligible, inducing a general compression of the structure. The actuated bending angle is smaller with a body printing laser velocity of $16\,mm\,s^{-1}$ than with a velocity of $14\,mm\,s^{-1}$, where the maximum of the experimental range is reached. Here, looking at the printed structures on the microscope images in Figure 5d, it is be observed that the active part compresses radially but does not induce a flexion of the overall structure because of its relative softness. More, the strong deformation of the originally cubic structures makes its measurement difficult. Toward structures based on the assembly of voxels, these parasitic radial compression and loss of planarity are strong limitations. As for the bilayer, the bending angle is measured for the bending voxel on two samples (Figure 5e). Here, the maximal values are reached when the ratio between the degrees of reticulation of the body and reinforcements is maximal, with $\theta_b = 19.5°$, $k_b = 8.5\,mm^{-1}$, and $\varepsilon_b = -17\%$. The hypothesis is that the thinner backbone of the bending voxel, compared to the bilayer voxel, strongly decreases its second moment of area I. Consequently, even if the stiffness E of the backbone increases, the bending stiffness EI does not increase sufficiently to limit the bending. It is important to observe that, at a printing velocity of $16\,mm\,s^{-1}$, the reticulation limit is approached, and the results are poorly repeatable between prints. Toward reliable voxels fabrication, choosing a body laser velocity of $14\,mm\,s^{-1}$ with the same reinforcement printing velocity could be considered preferable as it improves the repeatability of the deformation without significantly reducing its amplitude. Compared to bilayer voxels, no parasitic deformation of the top face is observed: it remains in a single plane for the bending voxel, where a discontinuity is observed between the active part and the reinforcement for the bilayer. This validates the voxel design for further assembly. For the compression voxel, as represented in Figure 5f, the actuation strain is computed as $\varepsilon_c = (L - L_0)/L_0$, with L and L_0 the actuated and initial lengths of a voxel side. The maximal strain ($\varepsilon_c = -37.1\%$) is obtained for laser velocities of $12\,mm\,s^{-1}$ for the reinforcement and $9\,mm\,s^{-1}$ for the body, but with an important variability between samples. A strain of $\varepsilon_c = -36.5\%$ is also obtained for a laser velocity of $16\,mm\,s^{-1}$ for the body. Contrarily to the bending and twisting actuator, and even if the effect is limited, the highest reinforcement printing laser velocity ($9\,mm\,s^{-1}$) maximizes the compression. The hypothesis is that stiffer reinforcements shrink less, limiting the structure compression. However, the effects of both printing

velocities have less influence on the compression strain as the absolute minimal strain is almost 20%. The results of the twisting voxels are shown in Figure 5g. Here, the angle is measured using the rod on the voxel. As for the bending voxel, the maximum deformation is obtained by maximizing the reticulation ratios: $\theta_t = 16.5°$ and $\gamma_t = -14.4\%$. Finally, the shear voxels results were not considered conclusive. Even if theoretically achievable with the proposed design, no clear shear is observed (Figure S3, Supporting Information) and therefore no measurement is made. In this case, the fabrication limitations discussed above can quickly impede the desired deformation. The results demonstrate that bending, compression, and twisting voxels can be obtained. More, toward their assembly, the bending structure shows better results than the classical bilayer, by minimizing the parasitic deformation. Considering all the basic kinematics, only elongation and shear are not obtained. Elongation is not achievable with shrinking material and shear can also be obtained indirectly, by combining two opposed bending voxels.

2.4. Advanced Kinematics

When assembling voxels into structures that can be actuated to generate complex motions, it is important to ensure that their configuration does not prevent their deformation by colliding with one another. Here, passive unpatterned and highly reticulated voxels can be added as links between active voxels. The printing time can also become limiting when printing multiple voxels, and the swelling during printing can be amplified, which induces a large displacement of the printed structure. To demonstrate the feasibility of using 2D imaging of the voxel assembly, two simple superstructures are designed: a bidirectional bending beam made of four aligned bending voxels; and a mirrored structure made of the assembly of one twisting, one passive, one compressive, and one bending voxel. The voxels are printed one by one. The order in which the elementary cubes are printed must be planned to ensure that each elementary cube is printed next to a previously printed voxel. **Figure 6**a shows the results for the bidirectional bending beam with the same printing parameters. Even if the expected S-shape is observed, the structure seems to have partially collapsed. Indeed, the base at the bottom of the picture shows a deflection, while it should stay fixed to the substrate. The different bending voxels also deform unequally because of fabrication irregularities and the collapsing of the structure. The twisting-compressive-bending structure is shown in Figure 6b, and a stop motion of its actuation can be found in Video, Supporting Information. The printing laser velocities are $4\,mm\,s^{-1}$ for the base and passive voxels, $5\,mm\,s^{-1}$ for the reinforcement, and $16\,mm\,s^{-1}$ for the active body. Despite defaults in the printed structures, the expected deformation is observed on each voxel and consequently on the overall structure. The total bending angle θ is 32°. This overall deformation corresponds to the sum of the bending and twisting angles of the voxels when actuated individually. It suggests that the assembly does not necessarily reduce the actuation strain of the individual voxels. Up to 14 voxels were printed in a single nonfunctional structure (Figure S4, Supporting Information). As a result of the long printing time, the swelling and the
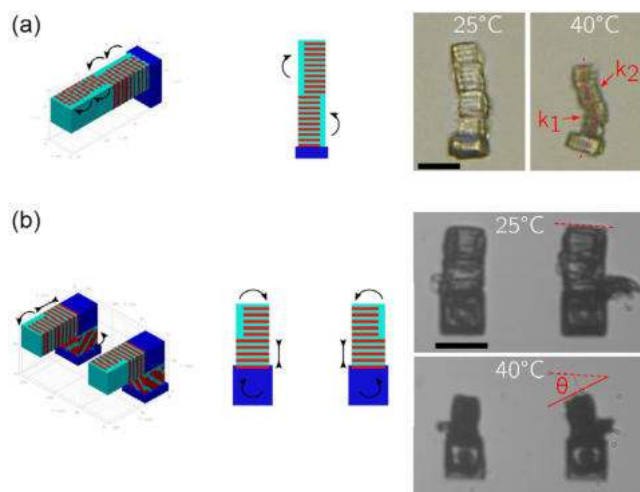
Figure 6. Complex structures. a) Bidirectional bending beam. Despite printing imperfections and a collapse on the substrate, the actuated S-shape and the change of curvature between k_1 and k_2 is observed. b) Twisting-compression-bending. The printed structure respects the designed geometry, even though a delamination defect can be observed on the right and deforms as expected when heated. The deflection angle θ is indicated for the right arm. Scale bar: 50 µm.

collapsing of the structure induced important inaccuracies. The main approach to overcome these limitations would be to adapt the machine parameters to minimize the printing time. In particular, the mechanical stage was used between each elementary cube for simplicity, which induced an important volume of twice-reticulated interfaces (overlaps). Using the piezo and galvo stages would also enable finer spatial resolution and high-speed printing. In addition, the resist formulation was not optimized to minimize the printing duration. For instance, increasing the proportion of photoinitiator could reduce the required exposure dose and therefore, the printing time. Similarly, the use of a lower magnification objective would increase the transmitted laser power and decrease the printing time.

3. Conclusion

This work contributes to the field of microrobotics by 1) adapting a two-photon-polymerization fabrication process to locally customize the printing parameters of structures, 2) characterizing the influence of the exposure dose and the temperature on the pNIPAM actuation strain, 3) validating voxels designs to generate bending, compression, and twisting, at the microscale using gray-tone lithography, and 4) demonstrating the possibility of generating advanced kinematics based on the proposed method. We reported in detail the fabrication process, as well as its challenges and limitations.

Bending, compression, and twisting voxels have been implemented using gray-tone lithography by adding adequate reinforcement to isotropically shrinking structures. They have been characterized in terms of deformation, and the influence of the exposure dose has been studied. The bending voxel was compared to the classical bilayer and achieved similar flexions (bending angle of 25° or curvature of $10\,\text{mm}^{-1}$) while reducing

the parasitic deformation. Similarly, the compression voxel reaches an actuation strain of 40%, and the twisting voxel bends up to 18°.

Here, we have not only demonstrated the ability to generate simple kinematics, but also the ability to combine them into complex 3D structures in a one-step fabrication process. The demonstrated structures would be difficult to achieve at this scale with another design and printing strategy, and the versatility of the voxel-based approach can be adapted to a large variety of motions.

Toward advanced microrobotics applications, the ability to achieve complex deformations does not necessarily imply functionality or the capacity to perform complex tasks such as gripping or locomotion. To this end, several limitations remain to be addressed in future work.

At the voxel level, the designs and material properties are not optimized. No shear deformation was observed experimentally, while the FEM indicated that it should be expected. We believe that a finer design, a more optimal exposure dose, and a better control of the fabrication process could lead to obtaining this deformation. Furthermore, no elongation can be obtained, which is more limiting. This is intrinsically made impossible because of the shrinking behavior of the pNIPAM. In addition, technical issues still limit the fabrication of large, collapse-free structures. Several approaches to overcome these limitations are presented in Section 2.4.

Adapted quantitative FEMs could be useful to optimize the designs and material choices to maximize a given deformation. This would require advanced material models, experimental validation, and the characterization of the influence of the temperature and the fabrication parameters on the actuation stress, the material stiffness, and its Poisson's ratio. Such optimization should not only aim at maximizing the desired deformation but also at minimizing the parasitic deformation of the voxels.

The possibility to actuate the voxels individually should be a key point of attention for future development. To achieve any task, the development of a reverse-engineering algorithm or method to guide the design of the assembly to achieve a given advanced kinematic would also be highly beneficial. This method should include guidelines to minimize or compensate for the parasitic deformations induced by the actuation of individual voxels.

The perspective to integrate other functionalities, such as self-healing, biodegradability, and sensing, is extremely appealing. At this scale, this should be implemented at the material level, for example, by incorporating (nano)fillers such as gold nanorods for light absorption, magnetic particles for additional actuation capabilities, or silica particles for color changes.

Finally, the generation of forces is required for microrobotics. Here, the forces have not been characterized but are expected to be at the micro-Newton scale, given the size of the structures and the softness of the hydrogel. At the transducer level, the actuation force depends on the material stiffness, the size of the actuator, and the actuation strain (through the contraction coefficient). Further work should focus on these different aspects to increase the actuation force. In particular, the material stiffness and the free actuation strain depend on the hydrogel chemistry, which has not been fully explored here. In addition, considering the implemented voxel actuators, a numerical model that properly captures the actuator behavior could open avenues to optimize

the voxel geometries to exert forces. It is important to note that the method introduced here, i.e., the decomposition of the complex motions into basic kinematics and their generation and assembly using the designed voxels, could be translated to any isotropically expansive or shrinking material/passive material couple.

4. Experimental Section

Materials: N-Isopropylacrylamide (NIPAM) (Sigma-Aldrich, > 97%), N, N-Methylenebis(acrylamide)' (BIS) (Sigma-Aldrich, Powder, > 99.5%), Lithium Phenyl(2,4,6-Trimethylbenzoyl)phosphinate (LAP) (TCI Europe, > 98%), Ethylene Glycol (Sigma-Aldrich, > 99%), 3-(trimethoxysilyl) propyl Methacrylate (Sigma-Aldrich, > 97%), Pentaerythritol Triacrylate (Sigma-Aldrich, > 97%).

Resist Synthesis: In a beaker, 2000 mg NIPAM, 200 mg BIS, and 2500 mg ethylene glycol were let to stir for at least 1 h until the NIPAM crystals were dissolved. 96 mg LAP was added to the mixture and again let to stir overnight, making sure to protect it from the daylight. Once completely dissolved, the resist was filtered using a 0.45 µm PTFE syringe filter and kept at room temperature in an opaque container. The experimental part was carried out in a clean room, in which UV-blocking filters allow the emission of light only above 500 nm. This avoids undesirable polymerization of the resin before printing.

Printing: The structures were printed with the Photonic Professional GT2 (PPGT2, Nanoscribe GmbH) system. The laser beam had a central wavelength of 780 nm and a pulse width of 80 fs at a repetition rate of 80 MHz. A 25×, NA = 0.8 objective was used in Dip-In laser lithography (DiLL) configuration with ITO-coated glass substrate. The ITO substrate was silanized before printing to increase the adhesion of the printed structure. In this process, the substrate was first cleaned using water, ethanol, and acetone. After drying, the substrate was activated with oxygen plasma for 60 s to make the substrate hydrophilic. The substrate was then placed for ≈1 h in a petri dish containing 30 mL ethanol mixed with 150 µL of 3-(trimethoxysilyl)propyl methacrylate. The substrate was then rinsed with acetone and distilled water and dried with air. The printing starts with the first layer printed 5 µm inside the substrate to ensure good adhesion with the substrate. The structures were observed on the substrate after rinsing the uncured resist with ethanol and directly placing it in a Petri box filled with distilled water. The structures must be kept in an aqueous environment. The laser power was set to 100%. The slicing and hatching distances were set to 0.5 µm. Three months after the printing, the structures stored in water showed strongly decreased deformation when actuated. Similarly, structures printed with old resist (more than 2 weeks) required a higher exposure dose to print correctly.

Gray-Tone Lithography: A versatile method was introduced to control the printing parameters locally. The structures were built as an assembly of elementary cubes of 5 µm side. These elementary cubes were sliced and hatched individually and then assembled by placing them adequately using the machines' slicer commands (DeScribe, Nanoscribe GmbH). To ensure good cohesion between these elementary cubes, an overlap of 1.5 µm (30% of an elementary cube side) between the cubes was added (Figure S1, Supporting Information). A too small or no overlap results in a detachment of the elementary cubes for the less reticulated parts during printing or actuation. A too large overlap would strongly increase the printing time for a given printed volume by increasing the volume exposed twice. Note that this printing strategy presents two disadvantages related to the use of the mechanical stage to move the axis between each elementary cube: it increases to total printing time (and hence raises swelling and adhesion issues, as described earlier) and limits the resolution to 0.5 µm, corresponding to the machine lateral resolution.

Imaging: A confocal microscope (Keyence VK-X200) with 10× and 50× objectives was used for precise imaging and measurement of the structures at room temperature (Figure 5c and 6a).

Voxels Characterization: A 1920 × 1200 pixels monochrome camera was used (uEye U3-306°CP-M-GL Rev.2, IDS) with a 15× objective (OPTEM

Zoom 125). A LED light source was added for transmission illumination, and the substrate was placed in a custom water bath. Two batches of structures were printed, and each measure was repeated by two different operators. The sources of measurement error were multiple and nonnegligible. The imprecision of the fabrication process was the main source of variability because of the loss of printability of the resists with time; the potential variability in the resist formulation; the evaporation of the solvent during long prints, which induces more concentrated resist; the swelling during printing; and the weak adhesion to the substrate. The measurement error (temperature, limited camera resolution, and image quality) and the difficulty to choose a reproducible and unambiguous reference on the not perfectly cubic structures must also be taken into account.

Modeling: COMSOL Multiphysics was used. Both active and passive parts were modeled by Young's modulus E, Poisson's coefficient ν, and their free actuation strain ε. The shrinking actuation strain was modeled by implementing a negative coefficient of thermal expansion (CTE) (α) for each material and a temperature step of 10 °C. The following values were used, as reported by Hippler et al.:[28] $E_{body} = 1$ kPa, $E_{reinforcement} = 11$ kPa, $\nu_{body} = \nu_{reinforcement} = 0.4$, $\alpha_{body} = -0.01$ K^{-1}, and $\alpha_{reinforcement} = -0.001$ K^{-1}. In addition, the heat capacity C_P, the thermal conductivity k, and the density ρ were imported from water. Using a Quasi-Static simulation and neglecting gravity, these last parameters do not influence the results. Concerning the boundary conditions, only the bottom face was considered to be fixed, and symmetry was used for bending, compression, and shear.

Supporting Information

Supporting Information is available from the Wiley Online Library or from the author.

Conflict of Interest

The authors declare no conflict of interest.

Data Availability Statement

The data that support the findings of this study are available from the corresponding author upon reasonable request.

[1] F. Soto, E. Karshalev, F. Zhang, B. E. F. de Avila, A. Nourhani, J. Wang, *Chem. Rev.* **2022**, *122*, 5365.

[2] M. Li, A. Pal, A. Aghakhani, A. Pena-Francesch, M. Sitti, *Nat. Rev. Mater.* **2021**, *7*, 235.

[3] L. Hines, K. Petersen, G. Z. Lum, M. Sitti, *Adv. Mater.* **2017**, *29*, 1603483.

[4] X. Kuang, D. J. Roach, J. Wu, C. M. Hamel, Z. Ding, T. Wang, M. L. Dunn, H. J. Qi, *Adv. Funct. Mater.* **2019**, *29*, 1805290.

[5] M. R. Lee, I. Y. Phang, Y. Cui, Y. H. Lee, X. Y. Ling, *Small* **2015**, *11*, 740.

[6] A. Nishiguchi, A. Mourran, H. Zhang, M. Möller, *Adv. Sci.* **2018**, *5*, 1700038.

[7] D. Jin, Q. Chen, T.-Y. Huang, J. Huang, L. Zhang, H. Duan, *Mater. Today* **2020**, *32*, 19.

[8] D. Martella, S. Nocentini, D. Nuzhdin, C. Parmeggiani, D. S. Wiersma, *Adv. Mater.* **2017**, *29*, 1704047.

[9] X. Wang, Z. Wei, C. Z. Baysah, M. Zheng, J. Xing, *RSC Adv.* **2019**, *9*, 34472.

[10] G. Decroly, A. Toncheva, L. Blanc, J. M. Raquez, T. Lessinnes, A. Delchambre, P. Lambert, *Actuators* **2020**, *9*, 131.

[11] C. Zhang, P. Zhu, Y. Lin, Z. Jiao, J. Zou, *Adv. Intell. Syst.* **2020**, *2*, 1900166.

[12] F. Connolly, C. J. Walsh, K. Bertoldi, *Proc. Natl. Acad. Sci. USA* **2017**, *114*, 51.

[13] G. Decroly, R. Raffoul, C. Deslypere, P. Leroy, L. Van Hove, A. Delchambre, P. Lambert, *Front. Robot. AI* **2021**, *8* 113.

[14] D. Guo, Z. Kang, Y. Wang, M. Li, *Smart Mater. Struct.* **2021**, *30* 095006.

[15] Y. Lin, G. Yang, Y. Liang, C. Zhang, W. Wang, D. Qian, H. Yang, J. Zou, *Adv. Funct. Mater.* **2020**, *30*, 2000349.

[16] R. Khodambashi, S. Berman, X. He, D. M. Aukes, in *IEEE 4th Int. Conf. on Soft Robotics, RoboSoft 2021*, IEEE, Piscataway, NJ **2021**, pp. 571–574.

[17] R. Khodambashi, Y. Alsaid, R. Rico, H. Marvi, M. M. Peet, R. E. Fisher, S. Berman, X. He, D. M. Aukes, *Adv. Mater.* **2021**, *33*, 10.

[18] X. Sun, L. Yue, L. Yu, H. Shao, X. Peng, K. Zhou, F. Demoly, R. Zhao, H. J. Qi, *Adv. Funct. Mater.* **2022**, *32*, 2109805.

[19] G. Adam, A. Benouhiba, K. Rabenorosoa, C. Clévy, D. J. Cappelleri, *Adv. Intell. Syst.* **2021**, *2000216*, 2000216.

[20] C. A. Spiegel, M. Hippler, A. Münchinger, M. Bastmeyer, C. Barner-Kowollik, M. Wegener, E. Blasco, *Adv. Funct. Mater.* **2020**, *30*, 26.

[21] W. Sun, S. Schaffer, K. Dai, L. Yao, A. Feinberg, V. Webster-Wood, *Front. Robot. AI* **2021**, 8.

[22] L. Tang, L. Wang, X. Yang, Y. Feng, Y. Li, W. Feng, *Progr. Mater. Sci.* **2021**, *115*, 100702.

[23] Z. Huang, G. Tsui, Y. Deng, C.-Y. Tang, *Nanotechnol. Rev.* **2020**, *9*, 1118.

[24] T.-Y. Huang, H.-W. Huang, D. D. Jin, Q. Y. Chen, J. Y. Huang, L. Zhang, H. L. Duan, *Sci. Adv.* **2020**, *6*, eaav8219.

[25] M. Hippler, E. Blasco, J. Qu, M. Tanaka, C. Barner-Kowollik, M. Wegener, M. Bastmeyer, *Nat. Commun.* **2019**, *10*, 232.

[26] Q. Ji, J. Moughames, X. Chen, G. Fang, J. J. Huaroto, V. Laude, J. A. I. Martínez, G. Ulliac, C. Clévy, P. Lutz, K. Rabenorosoa, V. Guelpa, A. Spangenberg, J. Liang, A. Mosset, M. Kadic, *Commun. Mater.* **2021**, *2*, 93.

[27] A. Nishiguchi, H. Zhang, S. Schweizerhof, M. F. Schulte, A. Mourran, M. Möller, *ACS Appl. Mater. Interfaces* **2020**, *12*, 12176.

[28] M. Hippler, Ph.D. Thesis, Karlsruher Institut für Technologie, **2020**.

[29] Y. Tao, C. Lu, C. Deng, J. Long, Y. Ren, Z. Dai, Z. Tong, X. Wang, S. Meng, W. Zhang, Y. Xu, L. Zhou, *Micromachines* **2022**, *13*, 32.

[30] C. Lv, X. C. Sun, H. Xia, Y. H. Yu, G. Wang, X. W. Cao, S. X. Li, Y. S. Wang, Q. D. Chen, Y. D. Yu, H. B. Sun, *Sens. Actuators, B* **2018**, *259*, 736.

[31] H. Jia, E. Mailand, J. Zhou, Z. Huang, G. Dietler, J. M. Kolinski, X. Wang, M. S. Sakar, *Small* **2019**, *15*, 1803870.

[32] H. Zhang, L. Koens, E. Lauga, A. Mourran, M. Möller, *Small* **2019**, *15*, 46.

[33] I. Rehor, C. Maslen, P. G. Moerman, B. G. van Ravensteijn, R. van Alst, J. Groenewold, H. B. Eral, W. K. Kegel, *Soft Robot.* **2021**, *8*, 10.

[34] Y. W. Lee, H. Ceylan, I. C. Yasa, U. Kilic, M. Sitti, *ACS Appl. Mater. Interfaces* **2021**, *13*, 12759.

[35] NanoGuide, https://support.nanoscribe.com/hc/en-gb (accessed: August 2022).

[36] Q. Hu, G. A. Rance, G. F. Trindade, D. Pervan, L. Jiang, A. Foerster, L. Turyanska, C. Tuck, D. J. Irvine, R. Hague, R. D. Wildman, *Addit. Manuf.* **2022**, *51*, 102575.

[37] Y. Hu, Z. Wang, D. Jin, C. Zhang, R. Sun, Z. Li, K. Hu, J. Ni, Z. Cai, D. Pan, X. Wang, W. Zhu, J. Li, D. Wu, L. Zhang, J. Chu, *Adv. Funct. Mater.* **2020**, *30*, 1907377.